World Conference on Timber Engineering Oslo 2023

DETERMINATION OF THE EFFECTIVE WIDTH OF CROSS-LAMINATED TIMBER RIB PANELS USING DIGITAL IMAGE CORRELATION

Miriam Kleinhenz[1], Martin Viertel[2], Thomas Demschner[3], Andrea Frangi[4]

ABSTRACT: The effective width of cross-laminated timber rib panels is analysed. The floor system consists of cross-laminated timber plates rigidly bonded to glued-laminated timber ribs by means of screw-press gluing. Ultimate-load tests were performed on four different cross-sections. Digital image correlation was used to visualize and monitor the strain distribution on top of the cross-laminated timber plates at midspan. The longitudinal strain distributions along the cross-laminated timber width were obtained for the determination of the effective width. The experimental results are compared to numerical results of a finite element model and to Eurocode 5 estimations. The longitudinal strain distributions show good agreement and confirm digital image correlation as a suitable measurement technique.

KEYWORDS: Massive timber rib panel, cross-laminated timber, effective width, optical measurement technique, finite-element modelling, strain distribution

1 INTRODUCTION

Long-span floor systems are required for building types such as commercial office buildings, residential buildings, schools, and industrial buildings. As a long-span floor system with spans up to 16 m, cross-laminated timber rib panels consist of cross-laminated timber (CLT) plates connected to glued-laminated timber (glulam) ribs. Full composite action is provided by a rigid connection between the composite components by means of screw-press gluing [1] (Figure 1).

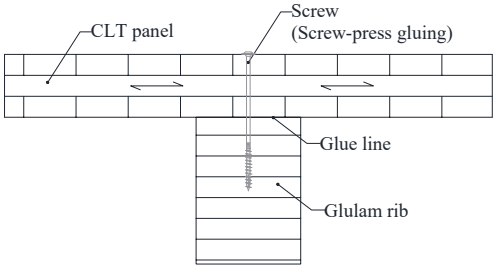

Figure 1: *Cross-section of cross-laminated timber rib panels.*

For such ribbed cross-sections, the assumption that the cross-section remains plane is incorrect. The simple beam theory according to Euler-Bernoulli is not applicable because the strains in the flange vary with the distance from the rib due to the in-plane shear flexibility of the flange. This leads to a non-uniform distribution of the longitudinal strains along the CLT width.
In a research project, ultimate-load tests were performed for the analysis of the structural behaviour. The system's stiffness and the resulting effective width were analysed [2]. This paper focuses on the strain distributions on top of the CLT plate being monitored during the ultimate-load tests using digital image correlation (DIC). The longitudinal strains obtained from the DIC measurements are compared to the numerical results of a finite element (FE) model. Both methods were validated by the measurements at midspan of a linear variable differential transformer (LVDT). Of both methods, the resulting effective widths are compared to the estimated effective width of Eurocode 5 [3].

2 SIMPLIFIED DESIGN METHOD

For simplified structural analysis, the effective width defines an equivalent cross-section that provides the same maximum bending stress and effective bending stiffness as the actual cross-section [4]. Figure 2 illustrates how the non-uniform stress distribution over the entire CLT width is replaced by a uniform stress distribution in the region of the effective width b_{ef}. Equation (1) shall apply:

$$\sigma_{x,max}(z) \cdot b_{ef} = \int \sigma_x(y,z)dy \qquad (1)$$

where $\sigma_{x,max}(z)$ is the maximum longitudinal bending stress distribution along the thickness of the CLT plate at rib centre, b_{ef} is the effective width, and $\int\sigma_x(y,z)dy$ is the integral of the longitudinal bending stresses along the thickness and along the width of the CLT plate.
The chapter on CLT design in the final draft [5] for a revised version of the European design standard for timber structures EN 1995-1-1 (Eurocode 5) [3] proposes simplified equations to estimate the effective width for

[1] Miriam Kleinhenz, Chair of Structural Engineering - Timber Structures, Institute of Structural Engineering, ETH Zurich, Switzerland, kleinhenz@ibk.baug.ethz.ch
[2] Martin Viertel, Bauhallenteam, Institute of Structural Engineering, ETH Zurich, Switzerland, viertel@ibk.baug.ethz.ch
[3] Thomas Demschner, Stora Enso Wood Products GmbH, Austria, thomas.demschner@storaenso.com
[4] Andrea Frangi, Chair of Structural Engineering - Timber Structures, Institute of Structural Engineering, ETH Zurich, Switzerland, frangi@ibk.baug.ethz.ch

https://doi.org/10.52202/069179-0319

ribbed plates build up from CLT plates. In the case of uniformly distributed loads, Equation (2) determines the effective width of Eurocode 5 $b_{ef,EC5}$:

$$b_{ef,EC5} = b_{rib} + \sum b_{ef,i} \tag{2}$$

$$= b_{rib} + b_{f,i} \cdot (0.5 - 0.35 \cdot \left(\frac{b_{f,i}}{l}\right)^{0.9} \cdot \left(\frac{(EA)_x}{(GA)_{xy}}\right)^{0.45})$$

where $b_{ef,i}$ is the effective width at each side of the rib width b_{rib}, $b_{f,i} = (b - b_{rib})$ is the clear rib distance, l is the span, and $(EA)_x/(GA)_{xy}$ is the ratio per meter width between the in-plane stiffness of the longitudinal CLT layers and the shear stiffness in plane of the gross CLT cross-section. The geometry is explained in Figure 3.

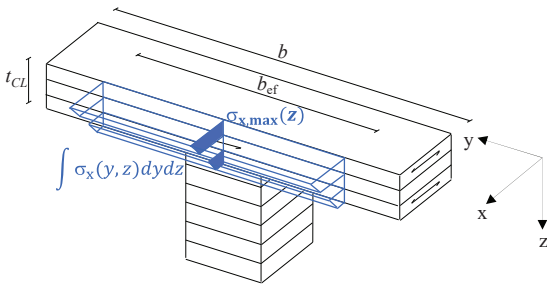

Figure 2: *Determination of the effective width.*

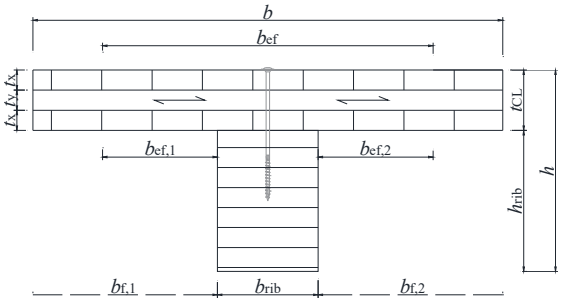

Figure 3: *Geometry of the cross-section.*

For the verification of stresses, the calculation method of rigidly bonded components (Bernoulli-beam) is applied. The calculation method is based on the assumption of full composite action between the CLT plate and glulam rib. The neutral axis is located in the centre of gravity of the composite cross-section z_s, determined by Equation (3):

$$z_s = \frac{\sum_{i=1}^{n+1}(E_i \cdot A_i \cdot a_i)}{\sum_{i=1}^{n+1}(E_i \cdot A_i)} \tag{3}$$

where E_i is the mean value of the modulus of elasticity of component i, A_i is its cross-section area, and a_i is the distance to its centroid from a selected origin.
The effective bending stiffness of the composite cross-section about the y-axis $(EI)_{ef}$ is defined by Equation (4):

$$(EI)_{ef} = \sum_{i=1}^{n+1}(EI)_i = \sum_{i=1}^{n+1}\left(\frac{E_i \cdot b_i \cdot h_i^3}{12} + E_i \cdot b_i \cdot h_i \cdot z_i^2\right) \tag{4}$$

where $(EI)_i$ is the bending stiffness of component i, E_i is the mean value of its modulus of elasticity, b_i is its width, h_i is its height, and z_i is the distance of its centroid to the global centre of gravity z_s.
The effective width b_{ef} defines the width b_i of n-longitudinal CLT layers (n = 1 for top CLT layer, n = 2 for second CLT layer etc.). Therefore, it is involved in both the determination of the global centre of gravity z_s, and the effective bending stiffness of the composite cross-section $(EI)_{ef}$. The rib is considered as (n+1)-component.

3 EXPERIMENTAL INVESTIGATIONS

3.1 CROSS-SECTIONS

Four cross-sections were tested, as presented in Figure 4 (A, B, C, and D), including T-sections (one CLT plate as top flange) and box-sections (CLT plates as top and bottom flanges). Twelve test specimens were tested using three replicates per cross-section (A1-A3, B1-B3, C1-C3, and D1-D3).

3.2 TEST SETUP AND PROCEDURE

The ultimate-load tests were performed as four point bending tests in accordance with EN 408 [6]. The test setup had a span l of 5.20 m (Figure 5). The span complies with the length of the horizontal furnace of later performed full-scale fire tests [2]. The test specimens were simply supported with a CLT width b of 0.933 m. Cross-sections B and D were tested without gypsum plasterboards. For bending at two points, two hydraulic cylinders applied the load uniformly with steel profiles of 200 mm depths along the test specimen's width.

3.3 MEASUREMENTS

Table 1 lists the measurements per test specimen. Load cells measured the applied cylinder forces F_{cyl}. At failure time, the maximum load per cylinder $F_{cyl,max}$ was on average 107 kN. The deflection w at midspan, as described in Figure 5, was recorded by the LVDT as w_{LVDT}. The maximum deflection $w_{LVDT,max}$ was on average 41 mm. The failure led in the linear-elastic load-deflection behaviour to a significant load drop.
An Optotrak Certus position sensor (NDI) was installed to record the local deflection on the front of the test specimen. NDI markers were fixed on the surface of the test specimen, which allowed for a 3D tracking of these markers throughout the testing. Their locations are shown in Figure 5. One NDI marker was located at the bottom edge at midspan. The LVDT at midspan confirmed the accuracy of this NDI measurement. To determine the local effective bending stiffness in the shear-free zone, further markers were placed on the front side of the test specimen below the force application points at a distance l_1 of 1.26 m according to EN 408 [6].

https://doi.org/10.52202/069179-0319

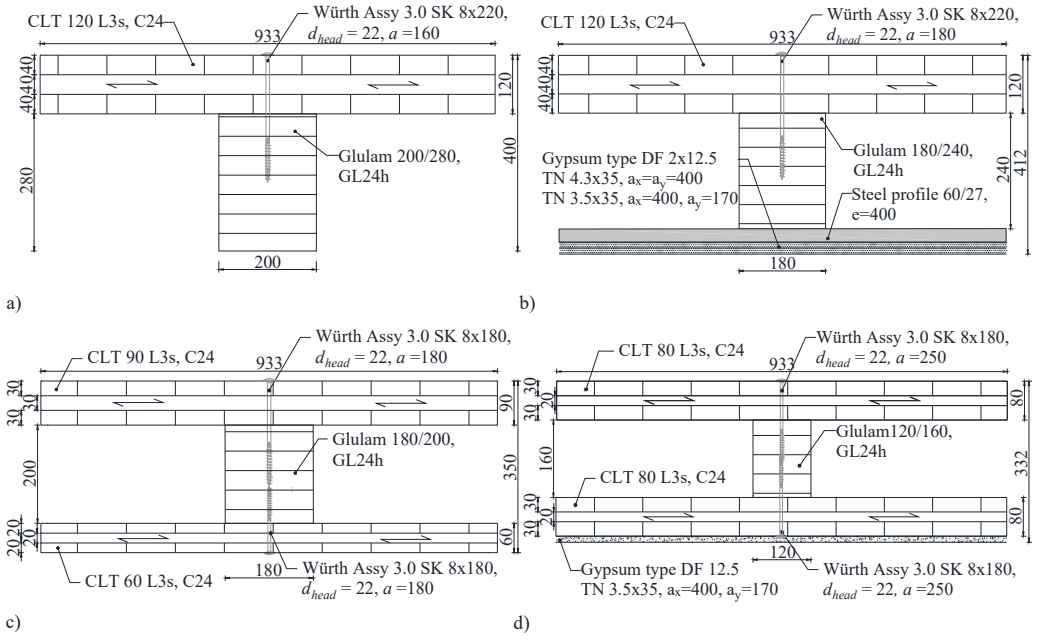

Figure 4: *Cross-section types of the experimental program, in [mm]: a) T-section (A); b) T-section initially protected (B); c) Box-section (C); d) Box-section initially protected (D).*

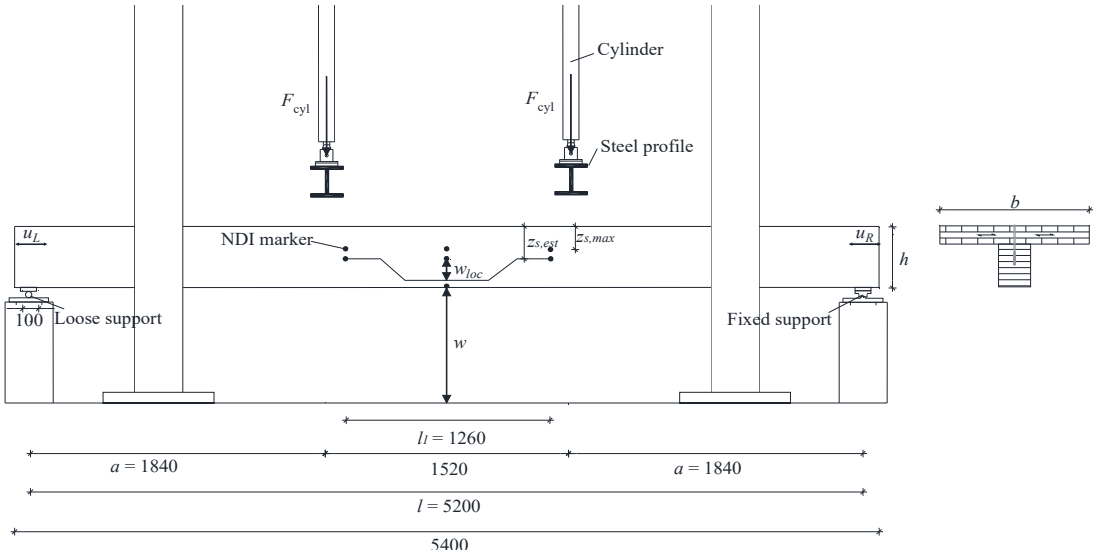

Figure 5: *Test setup in accordance with EN 408* ***[6]****.*

Over the height of the test specimen, these markers were located at two estimated positions of the neutral axis (= global centre of gravity): at $z_{s,max}$ for the maximum system (width b), and at $z_{s,est}$ for the estimated system according to Equation (2) (width $b_{ef,EC5}$). As the actual position can be assumed to be within these limits, the mean on both cases was calculated as local deflection w_{loc}. At failure, the maximum local deflection $w_{loc,max}$ was on average 2.2 mm.

3.4 EXPERIMENTAL RESULTS

3.4.1 Experimental effective bending stiffness

A linear regression was used to determine the slope of the load-deflection curve $\Delta F/\Delta w_{loc}$ [7]. In accordance with EN 408 [6], the experimental effective bending stiffness was calculated as local effective bending stiffness $(EI)_{ef,l}$ according to Equation (5):

$$(EI)_{ef,l} = \frac{a \cdot l_1^2}{16} \frac{\Delta F}{\Delta w_{loc}} = \frac{a \cdot l_1^2}{16} \frac{(2\Delta F_{cyl})}{\Delta w_{loc}} \quad (5)$$

https://doi.org/10.52202/069179-0319

Table 1: *Experimental measurements and results per test specimen – Maximum load per cylinder, ultimate load including self-weight, corresponding maximum deflection measured by the LVDT and maximum local deflection, local effective bending stiffness, experimental effective width, and maximum experimental bending stress on top of the top CLT plate.*

Test specimen	Cross-section type	$F_{cyl,max}$	F_{max}	$w_{LVDT,max}$	$w_{loc,max}$	$(EI)_{ef,l}$	$b_{ef,test}$	$b_{ef,test}/b$	$\sigma_{max,test}(z_{top})$
		[kN]	[kN]	[mm]	[mm]	[MNm^2]	[m]	[-]	[N/mm^2]
A1	T	180	363	53	2.7	24.2	0.92	0.98	-26.4
A2*		88	181	31	1.5	20.9	0.90	0.96	-14.3
A3		106	216	38	2.1	19.1	0.74	0.79	-19.9
B1*		93	190	46	2.9	12.8	0.73	0.78	-23.3
B2		78	160	42	2.5	12.2	0.63	0.68	-20.7
B3		76	156	38	2.3	12.0	0.65	0.70	-19.5
C1*	Box	102	208	34	1.8	20.9	0.80	0.86	-19.3
C2		147	298	52	2.7	20.7	0.74	0.80	-29.4
C3		110	224	38	2.1	19.9	0.74	0.79	-22.1
D1		112	228	43	2.2	18.7	0.71	0.76	-24.7
D2		99	202	38	2.0	18.1	0.68	0.73	-22.6
D3*		98	200	37	2.0	18.0	0.72	0.77	-21.5
mean		107	219	41	2.2	18.1	0.75	0.80	-22.0
SD		28	56	6.4	0.4	3.7	0.08	0.09	3.7
CoV		0.26	0.26	0.16	0.17	0.20	0.11	0.11	0.17

* Selected test specimens for the DIC technique.

where l_1 is the gauge length for the determination of modulus of elasticity, and a is the distance between support and force application, as shown in Figure 5.
Table 1 lists the local effective bending stiffness $(EI)_{ef,l}$ per test specimen; on average 18.1 MNm^2.

3.4.2 Experimental effective width

Due to the correlation between the effective bending stiffness $(EI)_{ef}$ and the effective width b_{ef}, the experimental effective widths $b_{ef,test}$ per test specimen were calculated by equating Equation (4) to the local effective bending stiffness $(EI)_{ef,l}$ of Table 1. A solve-function of nonlinear equations was used. Table 1 lists the experimental effective widths $b_{ef,test}$ per test specimen. Here, the experimental effective width $b_{ef,test}$ defines the width b_i of the longitudinal CLT layers of the top and bottom CLT plate.
Figure 6 presents the results in relation to the CLT width b. In addition, estimated effective widths of Eurocode 5 $b_{ef,EC5}$ were calculated according to Equation (2). Since no formula is given for loading in bending at two points, the formula for uniformly distributed loads was used. For box-sections, an average value of the top and bottom CLT plate is given. While the experimental effective width $b_{ef,test}$ was on average 80% of the CLT width, it would have been estimated at 60% by Eurocode 5 ($b_{ef,EC5}$).

3.4.3 Maximum experimental bending stress

Based on the calculation method of rigidly bonded components, the maximum experimental bending stress on top of the top CLT plate $\sigma_{max,test}(z_{bot})$ is calculated according to Formula (6):

$$\sigma_{max,test}(z_{top}) = \frac{M_{max} E_{CLT}}{(EI)_{ef,l}} \cdot (z_1 + \frac{h_1}{2}) \quad (6)$$

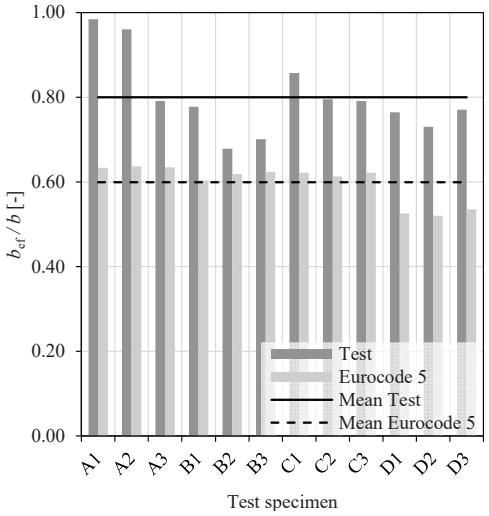

Figure 6: *Experimental and by Eurocode 5 estimated effective width of the tests specimens in relation to the CLT width.*

With

$$M_{max} = F_{max}/2 \cdot a \quad (7)$$

where E_{CLT} is the modulus of elasticity of the top CLT plate, $(EI)_{ef,l}$ is the local effective bending stiffness (Table 1), and h_1 and z_1 are the height and the distance to the global centre of gravity z_s according to Equation (3) of the top CLT layer, and a is the distance between support and force application, as shown in Figure 5. The ultimate load F_{max} includes the self-weight of the test specimen (see Table 1). The modulus of elasticity of the top CLT plate E_{CLT} and the dimensions of the single CLT plates and glulam ribs have been measured in advance and were

https://doi.org/10.52202/069179-0319

taken from [7]. Table 1 lists the maximum experimental bending stress on top of the top CLT plate $\sigma_{max,test}(z_{bot})$ per test specimen. At failure, the compressive stress value was on average 22 N/mm^2. The top side of the top CLT plate was under compression.

4 DIGITAL IMAGE CORRELATION

4.1 TEST SETUP AND PROCEDURE

In [8], LVDTs were installed at midspan side by side along the CLT width to measure the deformations on the CLT surface. Digital image correlation (DIC) is an optical measurement technique to capture relative 3D changes in sequential images. In this research project, the DIC technique was used at midspan to obtain the strain field distributions on top of the CLT plate of four selected test specimens (A2, B1, C1, and D3). Therefore, a rectangular area of interest of around 1.17 m^2 (0.90 m x 1.30 m) was observed between the two cylinders of the test setup (Figure 7). In the area of interest, a regular, black speckle pattern was applied with a paint roller on top of a white undercoat (speckle size: 1.8 mm). The contrast between speckle and undercoat improves the analysis' accuracy [9,10]. To improve the analysis' quality, LED floodlight illuminated the area of interest.

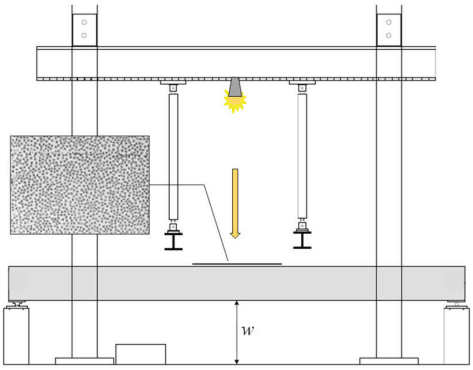

Figure 7: *Test setup in accordance with EN 408* ***[6]*** *including the measurements of the digital image correlation at midspan (area of interest).*

Digital images were simultaneously taken using a set of two cameras, type FLIR, Grasshopper 3, 12.3 MP. The resolution obtained was 4096x3000. The cameras were attached to the universal testing machine by an additional support frame with a distance to the area of interest of approximately 2.20 m. The baseline between the cameras and the distance between the cameras and the test specimen were checked after calibration of the DIC system. Digital images were taken during the ultimate-load tests (frame rate: 30 fps). In a zero-displacement test, the correlation error was checked in dependency of the speckle size, and the subset size. A subset size of 45 pixels on average was used for the image correlation. Displacements were calculated from the digital images by the comparison of virtual subsets containing a certain amount of pixels in original and deformed states at different instants of time. Therefore, a reference image was chosen that was taken in the unloaded phase. Since the projection error did not exceed the value of 0.1, the test specimen's movement or its distance to the cameras remained small. For the calculation, the origin of a coordinate system was set in the centre of the test specimen, thus in the middle of the area of interest. The software VIC-3D Digital Image Correlation Version 9.1.6 [11] was used for calibration, collection of digital images, running the correlation, and calculation of the displacements.

4.2 VALIDATION

The DIC measurements of the four selected test specimens were validated by comparing the maximum vertical displacements $w_{DIC,max}$ at the centre of the area of interest with the maximum deflections measured by the LVDT $w_{LVDT,max}$ (Figure 8). The results show perfect correlation.

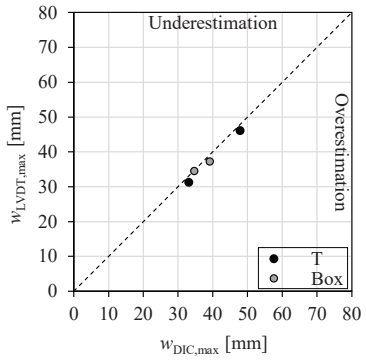

Figure 8: *Maximum deflections - Experimental results measured by the digital image correlation (DIC) and by the linear voltage displacement transducer (LVDT).*

5 NUMERICAL INVESTIGATIONS

5.1 FINITE ELEMENT MODEL

The modelling framework is developed using the Python programming language [12] and Abaqus Unified FEA software suite for finite element analysis [13]. The cross-section of a T-section was sketched and extruded to one deformable part. A geometric symmetry simplification was considered in the form of a vertical symmetry plane in the middle of the cross-section in longitudinal direction and a vertical symmetry plane at midspan (Figure 9). The support was defined as roller support. The generated part was partitioned into flange and rib. The flange was partitioned into the CLT layers, the material orientations of which were defined by local coordinate systems. The contact interactions between flange and rib, and the CLT layers were considered as rigid. The flexible-in-shear multi-layered FE model was loaded as four point bending test. As in the test setup, the mechanical load was applied uniformly at the position of the cylinder along the CLT width over a depth of 200 mm. A gravity load could be activated using a gravity acceleration of 9806.65 mm/s^2. Based on a sensitivity study [14], a mesh of 20x20 mm^2 was chosen. The incompatible mode eight-node brick element (C3D8I) was used for the analyses. Material properties were discussed as linear-elastic and orthotropic using the material properties of Table 2 for the nine engi-

https://doi.org/10.52202/069179-0319

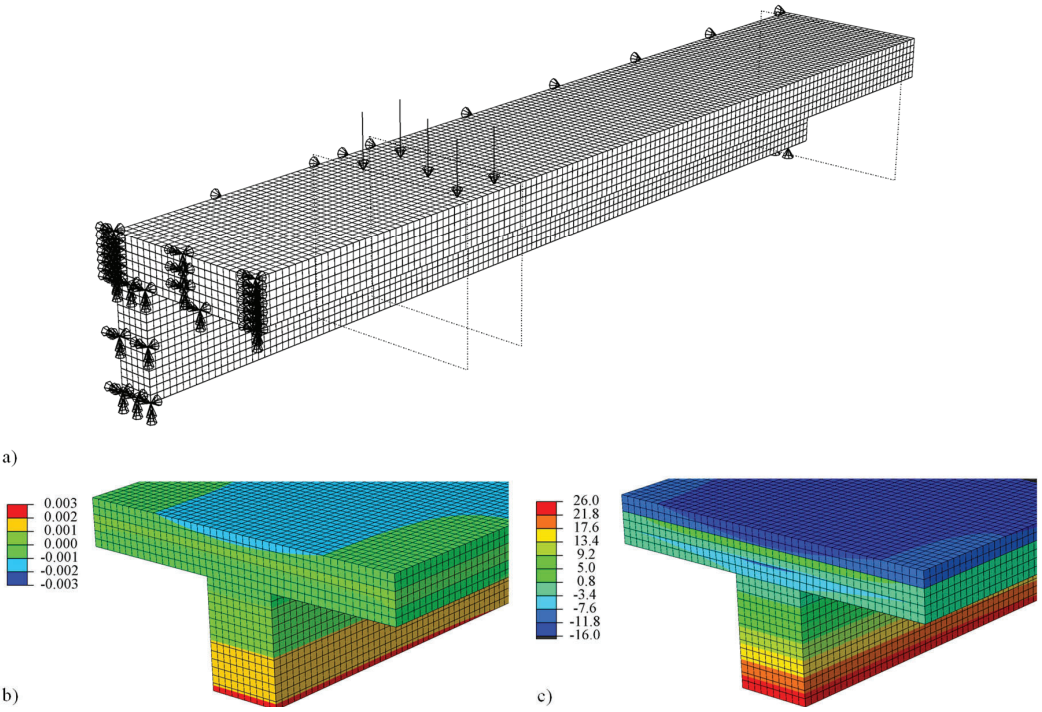

Figure 9: *Finite element model and numerical results mirrored by the vertical symmetry plane (b) and c)): a) 3D FE model; b) Longitudinal strains at midspan, in [-]; c) Longitudinal stresses at midspan, in [N/mm²].*

Table 2: *Material properties for CLT [6] and glulam [17].*

Material	Class	E_x	E_y	E_z	G_{xy}	G_{xz}	G_r	ν_{xy} [2)]	ν_{xz} [2)]	ν_{yz} [2)]
		[N/mm²]	[N/mm²]	[N/mm²]	[N/mm²]	[N/mm²]	[N/mm²]	[-]	[-]	[-]
CLT	CLT24	12500 [1)]	450	450	Eq. (8)	650	Eq. (9)	0.395	0.395	0.410
Gluam	GL24h	11500	300	300	650	650	65	0.395	0.395	0.410

[1)] Value given by Stora Enso.
[2)] Values based on Bodig and Jayne [15].

neering constants. The materials were assigned to the CLT layers as CLT and to the rib as glulam. The shear modulus in-plane of the gross CLT cross-section G_{xy} and the rolling shear modulus of CLT G_r were determined according to Equation (8) and Equation (9):

$$G_{xy} = min\left(\frac{650}{1 + 2.6 \cdot \left(\frac{t_l}{b_l}\right)^{1.2}}; 450\right) \quad (8)$$

$$G_r = min\left(30 + 17.5 \cdot \left(\frac{b_l}{t_l}\right); 100\right) \quad (9)$$

where t_l is the thickness of the lamination, and b_l is either the width of the lamination, the distance between the edge and a groove or the spacing between grooves within the lamination [16,17]. The latter was taken as average distance between grooves of the edge-bonded laminations, declared as 150 mm by Stora Enso.
The FE model was generated for each test specimen of the ultimate-load tests based on the specified dimensions, density, and the determined local modulus of elasticity as modulus of elasticity in x-direction E_x of the single components (CLT plates and glulam ribs), taken from [7]. The maximum load per cylinder $F_{cyl,max}$ was applied per test specimen (Table 1).

5.2 VALIDATION

The gravity load was deactivated in the FE model and the deflection at midspan was requested in the middle of the bottom edge in the post-processing. The FE model was validated by comparing the maximum numerical deflections $w_{sim,max}$ to the maximum deflections measured by the LVDT $w_{LVDT,max}$ (Figure 10). The results show good correlation with a coefficient value of 0.96.
Then, the gravity load was activated in the FE model. The flexible-in-shear multi-layered FE model resulted in a non-uniform stress distribution along the CLT width. On top of the CLT plate at midspan, the stress value in longitudinal direction at rib centre was requested from the created output database. Figure 11 presents per test specimen the maximum longitudinal stress values

https://doi.org/10.52202/069179-0319

$\sigma_{x,max,sim}(z_{top})$ of the FE model in comparison to the maximum experimental bending stresses $\sigma_{max,test}(z_{top})$ (Table 1). The results show good correlation with a coefficient value of 0.91.

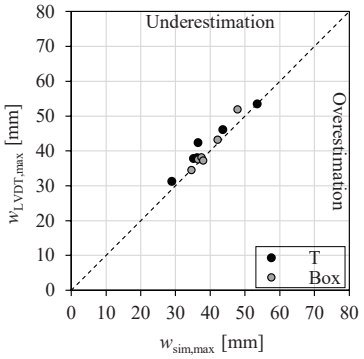

Figure 10: *Maximum deflections – Numerical results (sim) in comparison to experimental results measured by the linear voltage displacement transducer (LVDT).*

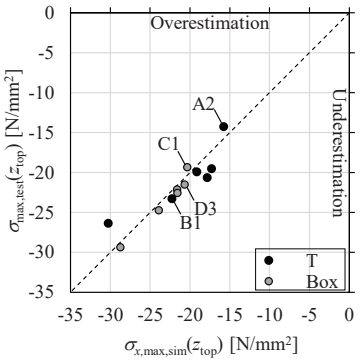

Figure 11: *Maximum stress values on top of the top CLT plate - Numerical results (sim) taken as longitudinal stress values at rib centre in comparison to experimental results (test) calculated as bending stresses according to Formula (6).*

6 RESULTS

6.1 STRAIN DISTRIBUTION

6.1.1 Digital image correlation

The DIC technique measured displacements on top of the top CLT plate. The software VIC-3D Digital Image Correlation Version 9.1.6 [11] was used for the determination of strains. The in-plane strains, i.e. longitudinal strains $\varepsilon_{xx,DIC}$, were calculated from the displacements as engineering strains. The accuracy was influenced by cracks and damages on the surface. Therefore, the longitudinal strains were averaged over the best illuminated region of the area of interest. Figure 12 presents the strain fields at failure of the selected test specimens. It should be noted that the region could only cover around 0.90 m of the CLT width *b* of 0.933 m.

Then, the averaged longitudinal strains $\varepsilon_{xx,DIC}$ were smoothed over the CLT width by taking the mean over a window length of 100 mm. Figure 13 presents the smoothed longitudinal strain distribution $\varepsilon_{xx,DIC}$ along the CLT width of the four selected test specimens (A2, B1, C1, and D3) at failure time. The strains result in compressive strains between 0.0006 and 0.0014. The results indicate a non-uniform stress distribution along the CLT width of the ribbed cross-sections.

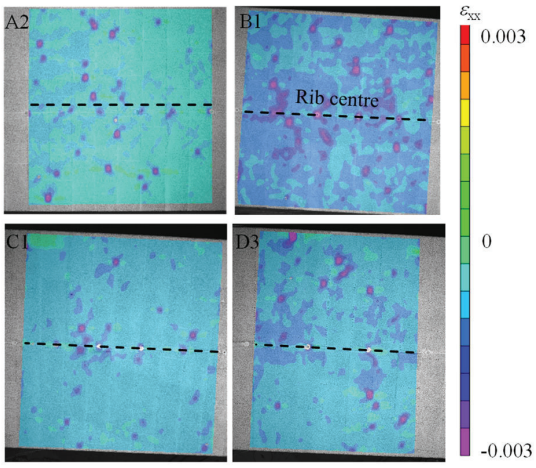

Figure 12: *Strain field on top of the top CLT plate at midspan - Longitudinal strains measured by the digital image correlation (DIC) of the four selected test specimens (Digital image at failure, contour range: -0.003 – 0.003 [-]).*

6.1.2 Finite element model

The gravity load was deactivated in the FE model. For comparison with the DIC results, the strains in longitudinal direction $\varepsilon_{xx,sim}$ along the CLT width were requested on top of the top CLT plate at midspan from the created output database (Figure 13). The strains result in compressive strains between 0.0008 and 0.0016. The flexible-in-shear multi-layered FE model resulted in a non-uniform stress distribution along the CLT width.

6.2 MAXIMUM STRAIN AND STRESS

The strains on top of the top CLT plate vary with the distance from the rib due to the in-plane shear flexibility of the flange. At rib centre, both the maximum longitudinal strain as well as the maximum stress value occur. Table 3 lists the results at midspan based on the DIC measurements and the FE model. The maximum longitudinal strain value at rib centre $\varepsilon_{xx,max}$ resulted on average in -0.00116 for the DIC measurements and in -0.00147 for the FE model. Figure 14 compares the maximum stress values on top of the top CLT plate at rib centre $\sigma_{x,max}(z_{top})$ between the FE model and the DIC measurements. The maximum stress value in longitudinal direction $\sigma_{x,max,sim}(z_{top})$ was requested from the created output database, as in Figure 11. The maximum stress value of the DIC measurements $\sigma_{x,max,DIC}(z_{top})$ was calculated by multiplying the maximum longitudinal strain value at rib centre $\varepsilon_{xx,max,DIC}$ with the modulus of elasticity of the top CLT plate $E_{CLT,}$ taken from [7]. The maximum stress value on top of the top CLT plate at rib centre $\sigma_{x,max}(z_{top})$ resulted in a compressive stress of on average 15.7 N/mm² for the DIC measurements and 19.8 N/mm² for the FE model.

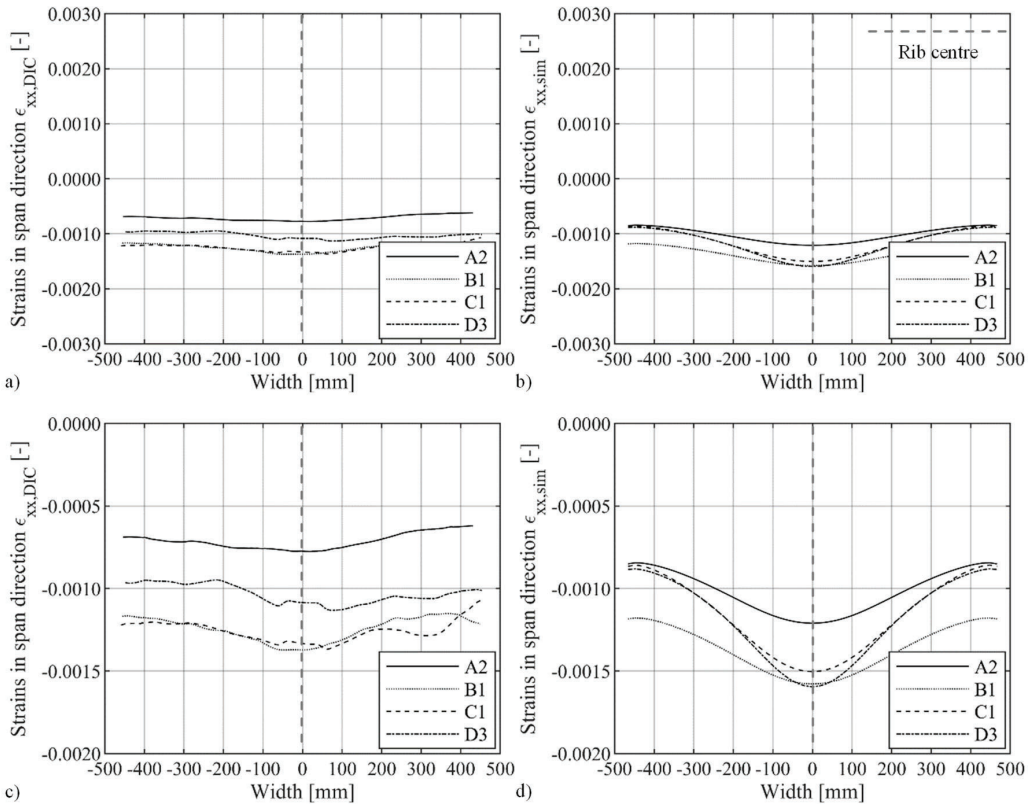

Figure 13: *Strain field distributions on top of the CLT plate - Longitudinal strains along the CLT width of the four selected test specimens a)+c) measured by the digital image correlation (DIC); b)+d) taken from the created output database of the FE model.*

Table 3: *Results based on the DIC measurements and the FE model (sim) per test specimen – Maximum longitudinal strain at rib centre, modulus of elasticity of the top CLT plate, and maximum bending stress and effective width on top of the top CLT plate.*

Test specimen	$\varepsilon_{xx,max,DIC}$	$\varepsilon_{xx,max,sim}$	E_{CLT}[1)]	$\sigma_{x,max,DIC}(z_{top})$	$\sigma_{x,max,sim}(z_{top})$	$b_{ef,top,DIC}/b$	$b_{ef,top,sim}/b$
	[-]	[-]	[N/mm²]	[N/mm²]	[N/mm²]	[-]	[-]
A2	-0.00078	-0.00121	12936	-10.0	-15.7	0.87	0.85
B1	-0.00137	-0.00158	14008	-19.2	-22.3	0.88	0.87
C1	-0.00137	-0.00150	13563	-18.6	-20.3	0.89	0.80
D3	-0.00113	-0.00160	13329	-15.1	-20.7	0.88	0.80
mean	-0.00116	-0.00147	13459	-15.7	-19.8	0.88	0.83
SD	0.00024	0.00016	388	3.7	2.5	0.01	0.03
CoV	-0.21	-0.11	0.03	-0.23	-0.12	0.01	0.04

[1)] Values taken from [7].

6.3 EFFECTIVE WIDTH

In this paper, longitudinal strains ε_{xx} were obtained at midspan only on the top side of the top CLT plate; for both the DIC technique and the FE model. Equation (10) shall apply in accordance with Equation (1) and Figure 2:

$$\varepsilon_{xx,max}(z_{top}) \cdot b_{ef,top} = \int \varepsilon_{xx}(y, z_{top})dy \qquad (10)$$

where $\varepsilon_{xx,max}(z_{top})$ is the maximum longitudinal strain value on top of the top CLT plate at rib centre, and $\int\varepsilon_{xx}(y,z_{top})dy$ is the integral of all longitudinal strains along the width of the CLT plate on top of the top CLT plate.

The effective width on top of the top CLT plate $b_{ef,top}$, is determined according to Equation (11):

$$b_{ef,top} = \frac{\int \varepsilon_{xx}(y, z_{top})dy}{\varepsilon_{xx,max}(z_{top})} \qquad (11)$$

The effective widths on top of the top CLT plate $b_{ef,top}$ were calculated for the four selected test specimens (A2, B1, C1, and D3) based on the longitudinal strains of the FE model and based on the DIC measurements. Table 3 lists the results in relation to the CLT width b. Figure 15 shows the comparison between the two models. Both the results of the DIC measurements and the FE model show

https://doi.org/10.52202/069179-0319

a low deviation between the results of maximum 4%. For the DIC results, the effective widths on top of the top CLT plate $b_{ef,top}$ resulted on average in 88% of the CLT width for all test specimens (CoV = 1%). For the numerical results, a distinction can be made between T-sections (86% of the CLT width) and box-sections (80% of the CLT width).

7 DISCUSSION

7.1 STRAIN DISTRIBUTION

The strain distributions along the CLT width on top of the top CLT plate are compared between DIC measurements and the FE model. The strain distributions show complete compression along the CLT width, as expected for the system of a simply supported beam under positive moment. The DIC results are in a range close to the expected range of the numerical results of the FE model. The DIC results of the T-sections (A2, B1) show good agreement in the shape of the strain distribution in comparison to the FE results. The DIC results of the box-sections (C1, D3) show a less pronounced decrease in strains with the distance from the rib centre. The composite system exhibited a lower shear lag effect as estimated by the FE model. Especially, the thinner top CLT plates of the box-sections proved to be less flexible in plane. The strain distributions at midspan might have been effected through a clinching effect of the steel profiles of the experimental test setup.

7.2 MAXIMUM STRAIN AND STRESS VALUE

The best fit can be seen for test specimen B1. Here, not only the shape of the strain distribution but also the maximum longitudinal strain value at rib centre $\varepsilon_{xx,max}$ comply between the DIC technique and the FE model. The FE model overestimates the maximum longitudinal strain value at rib centre $\varepsilon_{xx,max}$ by only 15%. For specimen A2, however, the FE model overestimates the value by 55%.

The maximum stress values on top of the top CLT plate at rib centre $\sigma_{x,max}(z_{top})$ are calculated from the maximum longitudinal strain value at rib centre $\varepsilon_{xx,max}$. Figure 14 outlines the overestimation by the FE model by up to 55%. The average error is 4.4 N/mm^2 (RMSE).

7.3 EFFECTIVE WIDTH

The effective widths on top of the top CLT plate $b_{ef,top}$ are in good agreement between the DIC technique and the FE model for the T-sections. The FE model underestimates the effective widths of the box-sections by 10%. This is based on the more pronounced non-uniform strain distribution along the CLT width. The small deviation between the results of the individual models (CoV ≤ 4%) illustrates the small influence of the material properties on the strain distribution. As outlined in [7], the effective width b_{ef} mainly depends on the stiffness of the floor system, e.g. the ratio of clear rib distance to span $b_{f,i}/l$, which was about 0.15 of the tested system.

Figure 15 puts the results in relation to the mean value of the estimated effective width of Eurocode 5 $b_{ef,EC5}$, taken from Figure 6. The effective width by Eurocode 5 $b_{ef,EC5}$ shows the approach on the safe side with an estimate of 60% of the CLT width on average.

Figure 15 puts the results in relation to the mean value of the experimental effective width $b_{ef,test}$, taken from Figure 6. The experimental effective width $b_{ef,test}$ was on average 80% of the CLT width. The higher deviation between the experimental results (CoV = 11%) illustrates the sensitivity of the experimental results based on the local deflections of less than 3 mm (see Table 1). The mean value of 80% of the CLT width complies well with the numerical investigations presented in [18]. There, the effective width would have been determined around 75% of the CLT width (Abb. 20, MM_Bsp3s_q).

The effective widths on top of the top CLT plate $b_{ef,top}$ of the DIC measurements and the FE model lay slightly above the mean value of the experimental effective width $b_{ef,test}$. It should be noted that the effective width b_{ef} of the entire flange or system is expected to be smaller than the effective width on top of the top CLT plate $b_{ef,top}$.

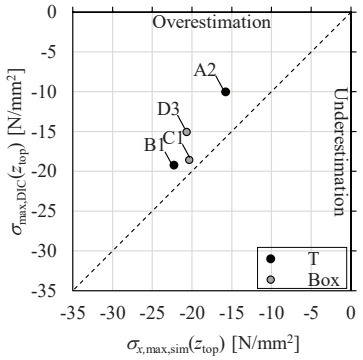

Figure 14: *Maximum stress values on top of the top CLT plate - Numerical results (sim) in comparison to results based on the DIC measurements (DIC).*

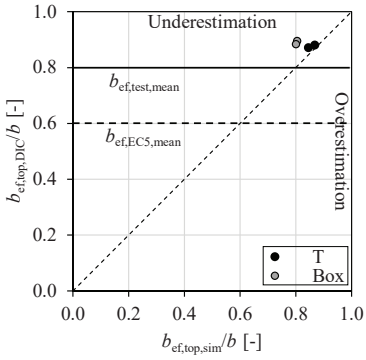

Figure 15: *Effective width - Results on top of the top CLT plate based on the FE model (sim) in comparison to the ones based on the DIC measurements (DIC); incl. mean values of the experimental and by Eurocode 5 estimated effective width.*

8 CONCLUSIONS

The DIC analysis allows visualizing the strain field on top of the CLT plate. In comparison to strain gauges and LVDTs, entire field measurements are possible. The proposed paper investigates DIC as a suitable measurement technique for the determination of the

effective width b_{ef}. The investigations apply to a floor system with a ratio of clear rib distance to span $b_{f,i}/l$ of about 0.15. The strain and stress distributions along the CLT width on top of the top CLT plate are compared between DIC measurements and the FE model. The DIC measurements and the numerical results of the FE model were validated against the experimental results of four tested cross-sections. Based on the DIC results, the composite system exhibited a lower shear lag effect as estimated by the FE model.

Although the in-plane stiffness was underestimated by the FE model, the results of the effective width on top of the top CLT plate $b_{ef,top}$ show good agreement between the DIC measurements and the FE model. Furthermore, the results comply with the effective width b_{ef} of the experimental results, which is on average 80% of the CLT width. Eurocode 5 gives an estimate on the safe side of 60% of the CLT width on average.

The numerical investigations formed the basis for thermo-mechanical investigations [7]. The aim was the determination of the effective width in fire over the entire height of the CLT plate. The 3D FE model resulted in a non-uniform, temperature-dependent strain distribution along the CLT width [19]. The temperature-dependent longitudinal bending stresses were taken along the CLT width and along the thickness of the longitudinal CLT layers per specified time step. A parametric study analysed the effective width in fire $b_{ef,fi}$ for a parameter range expected in practice.

ACKNOWLEDGEMENT

The authors gratefully acknowledge the financial and technical support by Stora Enso Wood Products GmbH in Ybbs, Austria. The numerical work has been supported by the students' work of Julian Brogli and Marco Lamberti.

REFERENCES

[1] K. Bratulic, M. Augustin, G. Schickhofer, Investigations concerning screw-press gluing of assemblies with CLT, in: International Network on Timber Engineering Research (INTER) – Proceedings of the 6th Meeting, Tacoma, USA, 2019.

[2] M. Kleinhenz, A. Just, A. Frangi, Experimental analysis of cross-laminated timber rib panels at normal temperature and in fire, Engineering Structures. 246 (2021) 113091. https://doi.org/10.1016/j.engstruct.2021.113091.

[3] EN 1995-1-1, Eurocode 5: Design of timber structures - Part 1-1: General - Common rules and rules for buildings, European Committee for Standardization (CEN), Brussels, 2004.

[4] S.P. Timoshenko, Strength of materials - Part II Advanced Theory and Problems, 2nd ed., D. Van Nostrand Company, inc., New York - Toronto - London, 1940.

[5] CEN/TC 250/SC 5 N 892: M515 SC5.T1 Phase 1 Final deliverables - SC5.T1 Final Document of prEN 1995-1-1 on CLT, CEN - CENELEC, Brussels, 2018.

[6] EN 408, Timber structures - Structural timber and glued laminated timber - Determination of some physical and mechanical properties, European Committee for Standardization (CEN), Brussels, 2012.

[7] M. Kleinhenz, Cross-laminated timber rib panels in fire, ETH Zurich, 2022. https://doi.org/10.3929/ETHZ-B-000577457.

[8] R. Masoudnia, A. Hashemi, P. Quenneville, Predicting the Effective Flange Width of a CLT Slab in Timber Composite Beams, J. Struct. Eng. 144 (2018) 04018084. https://doi.org/10.1061/(ASCE)ST.1943-541X.0001979.

[9] R.A. Freire, H. Di Benedetto, C. Sauzéat, S. Pouget, D. Lesueur, Crack propagation analysis in bituminous mixtures reinforced by different types of geogrids using digital image correlation, Construction and Building Materials. 303 (2021) 124522. https://doi.org/10.1016/j.conbuildmat.2021.124522.

[10] S.A. Hadigheh, R. McDougall, C. Wiseman, L. Reid, Evaluation of composite action in cross laminated timber-concrete composite beams with CFRP reinforcing bar and plate connectors using Digital Image Correlation (DIC), Engineering Structures. 232 (2021) 111791. https://doi.org/10.1016/j.engstruct.2020.111791.

[11] Correlated Solutions, Inc., VIC-3D Digital Image Correlation (Version 9.1.6), (2020).

[12] Python Software Foundation, Python (version 3.7), (2018). https://www.python.org/.

[13] Dassault Systemes, Abaqus FEA, (2019). https://www.3ds.com/products-services/simulia/products/abaqus/.

[14] P. Hodel, CLT Rib Panels - Simulation der Tragfähigkeit im Brandfall, Master thesis, ETH, 2021.

[15] J. Bodig, B.A. Jayne, Mechanics of wood and wood composites, Reprint ed., Krieger Pub, Malabar, Fla., 1993.

[16] R. Brandner, G. Flatscher, A. Ringhofer, G. Schickhofer, A. Thiel, Cross laminated timber (CLT): overview and development, Eur. J. Wood Prod. 74 (2016) 331–351. https://doi.org/10.1007/s00107-015-0999-5.

[17] T. Ehrhart, R. Brandner, G. Schickhofer, A. Frangi, Rolling Shear Properties of some European Timber Species with Focus on Cross Laminated Timber (CLT): Test Configuration and Parameter Study, in: International Network on Timber Engineering Research (INTER) – Proceedings of the 2nd Meeting, ETH Zurich, Šibenik, Croatia, 2015. https://doi.org/10.3929/ETHZ-A-010548168.

[18] T. Bogensperger, Darstellung und praxistaugliche Aufbereitung für die Ermittlung mitwirkender Plattenbreiten von BSP-Elementen, Research Report focus_sts 2.2.3_1, Graz, Austria, 2013.

[19] M. Kleinhenz, A. Frangi, A. Just, The effective width of cross-laminated timber rib panels in fire, in: International Network on Timber Engineering Research (INTER) – Proceedings of the 9th Meeting, Bad Aibling, Germany, 2022.

https://doi.org/10.52202/069179-0319